Research Square

Preprints are preliminary reports that have not undergone peer review.
They should not be considered conclusive, used to inform clinical practice,
or referenced by the media as validated information.

Enhancing Mesenchymal Stem Cell Culture on Microcarriers in Spinner Flask via Impeller Design Optimization for Aggregated Suspension

Botao Zhang
East China University of Science and Technology State Key Laboratory of Bioreactor Engineering
Qiaohui Lu
East China University of Science and Technology State Key Laboratory of Bioreactor Engineering
Gance Dai
East China University of Science and Technology
Yi Zhou
East China University of Science and Technology State Key Laboratory of Bioreactor Engineering
Qian Ye
East China University of Science and Technology State Key Laboratory of Bioreactor Engineering
Yan Zhou (zhouyan@ecust.edu.cn)
East China University of Science and Technology State Key Laboratory of Bioreactor Engineering
Wensong Tan
East China University of Science and Technology State Key Laboratory of Bioreactor Engineering

Research Article

Keywords: Umbilical cord mesenchymal stem cells, Microcarrier suspension culture, Computational fluid dynamics, spinner flask, Flow field structure, Cell-microcarrier aggregate size

Posted Date: September 8th, 2023

DOI: https://doi.org/10.21203/rs.3.rs-3321432/v1

License: This work is licensed under a Creative Commons Attribution 4.0 International License.
Read Full License

Version of Record: A version of this preprint was published at Bioresources and Bioprocessing on December 3rd, 2023. See the published version at https://doi.org/10.1186/s40643-023-00707-7.

Abstract

Human umbilical cord-derived mesenchymal stem cells (hUC-MSCs) are widely utilized in the field of regenerative medicine, particularly in cell therapy and tissue engineering. However, their application and development are hindered by limitations in cell expansion efficiency. When hUC-MSCs are cultured in suspension while attached to microcarriers, they tend to aggregate, and adjusting operational parameters fails to resolve the conflict between shear and aggregation. The microenvironment created by the original impeller is not suitable for cell growth. In this study, computational fluid dynamics (CFD) simulations were employed to investigate the flow field structure generated by the original impeller in the commercial spinner flasks. It was found that the flow field structure were unsuitable for the expansion of cells prone to aggregate. Consequently, a new impeller was designed to alter the flow field structure, aimed to promote aggregate suspension while maintaining a similar shear rate at the same rotation speed. Compared to the original impeller, the newly designed impeller demonstrated significant improvements. Notably, it reduced the size of aggregates, increased maximum cell density, and preserved cell stemness during cell expansion. Combining simulation results with experimental data, this study reveals that the degree of suspension of aggregates played a critical role in determining aggregate size. Additionally, the level of cell stemness was determined by modulating shear rate and the degree of aggregate suspension.

Introduction

Since the initial discovery of human mesenchymal stem cells (hMSCs) in 1968(Friedenstein et al. 1968), their therapeutic potential in immunological modulation, tissue repair, and regenerative disorders has been widely recognized(Gregoire et al. 2017; Papaccio et al. 2017). Various adult tissues, including bone marrow, adipose tissue, umbilical cord, and skin, can serve as sources of hMSCs(Hoang et al. 2022; Lin et al. 2019). Among these, human umbilical cord-derived mesenchymal stem cells (hUC-MSCs) have garnered significant attention due to their easy access, reduced ethical considerations, low immunogenicity, and robust cytokine secretion capabilities(El Omar et al. 2014; Barberini et al. 2014). Despite their immense potential, the number of hUC-MSCs that can be isolated from a single umbilical cord is limited. Consequently, large-scale *in vitro* expansion is necessary to meet cell number requirements for a single intravenous injection, which typically ranges from 10^7 to 10^{10} cells(Sharma et al. 2014; Jo et al. 2014; Huang et al. 2018).

Numerous studies have highlighted that traditional static cell culture systems, such as cell factories, do not meet the demands of the current and future cell therapy market in terms of economic feasibility, stability, and safety(Simaria et al. 2014; Eibes et al. 2010). Therefore, the design of a microcarrier suspension-based bioreactor that enables stable large-scale *in vitro* expansion of hMSCs while preserving their proliferation and differentiation potential has emerged as a critical research direction(Eibes et al. 2010; Bin Hassan et al. 2020). Spinner flasks are commonly used bioreactors for hMSCs, in which cells attached to microcarriers aggregate during their growth. Over time, the size of these microcarrier-cell aggregates increases. Due to their rapid proliferation, strong adhesion, and migration capabilities, hUC-MSCs often form millimetre-sized aggregates before cell harvesting when microcarriers are poorly

suspended. The formation of such aggregates introduces mass transfer limitations that impact cell viability and make cell digestion and isolation challenging(Ferrari et al. 2012; Alanazi et al. 2019; Zeddou et al. 2010; Luo et al. 2014). Increasing the impeller speed of spinner flasks can enhance the degree of aggregate suspension and reduce the maximum size of aggregates(Jossen et al. 2016). However, this approach also leads to an increase in shear force(Zhang et al. 2022), which can either hinder hMSCs growth(Nienow et al. 2016) or dislodge hMSCs from the microcarriers(Nienow et al. 2014). hMSCs are sensitive to changes in their microenvironment, and exposure to intermittent high shear forces (0.42 Pa) during flow has been shown to significantly increase the expression levels of osteogenic genes, which is unfavourable for stem cell expansion(Jiao et al. 2022; Liu et al. 2012). Thus, achieving a balance between aggregate suspension and shear force exerted on cells attached to microcarriers is crucial to obtain controlled aggregate size during cell harvest, while minimizing the shear force applied to cells. Effectively managing these parameters is pivotal to enable the large-scale *in vitro* expansion of hMSCs.

To address the shear sensitivity and aggregation characteristics of hMSCs(Jossen et al. 2016; Zwietering 1958), critical rotational speeds (N_{S1} and N_{S1u}) are commonly used to guide microcarrier suspension cultures in current studies. N_{S1} represents the critical rotational speed that maintains the microcarrier fully suspended (non-uniformly suspended), while N_{S1u} represents the critical rotational speed that ensures the microcarrier is mobile. CFD has been proposed as a means to characterize the flow field and predict shear strain rate (SSR) distributions, which can be used to measure aggregate size(Zwietering 1958; Schirmaier et al. 2014). Jossen *et al.*(Jossen et al. 2016) explored stirring speeds ranging from 25–120 rpm in commercial spinner flasks with a working volume of 100 mL. Critical rotational speeds (N_{S1u} and N_{S1}) were found to be 49 and 61 rpm, respectively. At the N_{S1u} speed, hMSCs achieved the highest level of cell amplification (117-fold), with an average aggregate size similar to that obtained at a speed of 120 rpm, measuring 0.58 mm and 0.55 mm, respectively. By employing N_{S1} and N_{S1u} standards, researchers have previously achieved the highest level of hMSCs amplification in a 50 L bioreactor using microcarrier suspension cultures, with a total cell count of approximately 10^{10} cells and a 43-fold amplification(Schirmaier et al. 2014; Lawson et al. 2017). However, few studies have considered the maintenance of cell stemness at different rotational speeds, which undermines the significance of N_{S1} and N_{S1u} standards as a guide for the large-scale expansion of stem cells in current production processes.

Different sources of hMSCs exhibit varying physiological characteristics(Simões et al. 2013), with different tolerances to mass transfer limitations and SSRs. When increasing the rotational speed to the point where the aggregate size decreases and cell growth is no longer limited by mass transfer, the magnitude of SSR may surpass the tolerance range of hMSCs, indicating that altering impeller speed does not necessarily enhance hMSCs expansion factors. Indeed, it has been previously shown that changing the impeller speed does not enhance hMSCs amplification multiplicity(Ferrari et al. 2012; Kaiser et al. 2013). Current strategies to overcome this issue mainly involve the addition of fresh microcarriers(Ferrari et al. 2012) or the use of microcarriers with lower densities(Kaiser et al. 2013) to improve aggregate suspension and reduce size at a specific rotational speed and SSR level, thereby

resulting in higher cell densities upon harvest. However, optimizing the rotational speed alone fails to enhance hMSCs amplification multiplicity. These findings suggest that increasing the degree of aggregate suspension has potential to optimize cell culture outcomes, but that microcarrier-specific control strategies have limited effects on improving aggregate suspension. Additionally, the impeller structure (rectangular or triangular plates) may not provide an efficient suspension of aggregates. CFD simulations were performed to analyse the flow field generated by the original impeller inside a commercial spinner flask at varying rotational speeds and sizes. Regardless of the conditions, the flow field exhibited consistent characteristics, characterized by the presence of multiple vortices(da Silva et al. 2020; Berry et al. 2016; Ghasemian et al. 2020). This phenomenon could be one of the reasons impeding the original impeller's ability to effectively suspend cell aggregates and maintain a balance between aggregate size and shear forces. As a result, optimization of the impeller structure is required to achieve a robust suspension capability at the same SSR level. Due to the fact that approximately 50% of the total volume is occupied by the swept volume of the impeller, quantification of the impeller's suspension capacity for cell aggregates can be achieved by referencing the axial pumping rate (Q_z)(Huang et al. 2022), which is commonly used for helical impellers. Furthermore, it is critical to investigate the potential relationship between aggregate size, SSR, Q_z, cell number, and mass. Current literature predicts and explains aggregate size and cell culture outcomes based on the distribution of SSR and Kolmogorov length scales generated by different rotational speeds of the original impeller (Ghasemian et al. 2020). However, limited studies have explored the influence of impeller structure and the degree of aggregate suspension on these factors, hindering a more comprehensive exploration of optimization methods for cell culture processes.

This study initially aimed to investigate the impact of different rotational speeds on the growth, aggregate size, and maintenance of stemness in hMSCs using a commercial spinner flask. The findings of this study revealed that lower rotational speeds (< 45 rpm) resulted in the formation of several millimetre-sized aggregates due to microcarrier deposition, leading to mass transfer limitations and subsequent cell death. On the other hand, higher rotational speeds (> 45 rpm) were found to be unfavourable for cell proliferation and stemness maintenance. These results indicated that regulating cell culture solely by adjusting rotational speed is not sufficient; the engineering characteristics of the reactor must be tailored to the specific cell requirements. By conducting CFD simulations to analyse the flow field characteristics inside a commercial reactor, a novel impeller design was developed. This novel impeller aimed to achieve a similar mean shear rate (SSR_{ave}) as the original impeller, but with a higher mean pumping rate (Q_{zave}) and a flow field structure better suited for aggregate suspension at the same rotational speed. When compared to the original impeller, the application of the novel impeller for hUC-MSCs amplification resulted in a reduction of 67% and 56% in cell aggregate size at 30 rpm and 45 rpm, respectively, while increasing the maximum cell density across all speeds. Additionally, the novel impeller design upregulated the expression levels of stemness genes and downregulated the expression of differentiation-related genes, thus reducing spontaneous cell differentiation. Overall, this study combined experimental and simulation data to determine that the impeller's Q_z played a more significant role in

determining aggregate size compared to the shear rate. These findings provide valuable guidance to achieve better expansion of high-quality and -quantity seed cells.

Materials and Methods

In vitro culture of hUC-MSCs

Passage 2 hUC-MSCs (Sayer Biologics, HUXUC-01001) were cultured in DMEM medium (Gibco, 12800082, America) supplemented with 5% platelet lysate and 1% penicillin/streptomycin (Beyotime). Cells were maintained in an incubator at 37°C and 5% CO2, with medium replenished every two days. When cells reached 80–90% confluency, they were harvested using 0.25% trypsin-EDTA. Cells were cryopreserved at a concentration of 2×10^6 cells/mL and stored in liquid nitrogen. Prior to use, cells were thawed and cultured in 75 cm^2 T-flasks. Cells at passages 6 to 8 were used in these experiments.

Amplification of hUC-MSCs on microcarriers

A 125 mL spinner flask reactor was utilized for all experiments. The inner wall of the spinner flask was coated with 5% silicone oil to prevent microcarriers from adhering to the vessel surface. Following manufacturer's instructions, 100 mL of phosphate buffer solution and 2.5 g/L Cultispher-S microcarriers were added to each spinner flask, and fully hydrated overnight. After sterilization, the microcarrier was washed with fresh culture medium. hUC-MSCs were digested in T75 flasks with 0.25% trypsin-EDTA to obtain single-cell suspensions. Cells were initially seeded in the spinner flasks at a density of 5×10^4 cells/mL. Eight hours after inoculation, intermittent mixing at 45 rpm (5 min of mixing followed by 25 min of resting) was used to promote cell attachment. To investigate the influence of different stirring speeds on cell-microcarrier aggregates, four continuous stirring speeds (30 rpm, 45 rpm, 60 rpm, and 75 rpm) were investigated. All flask reactors were placed in an incubator at 37°C and 5% CO_2 for subsequent experiments.

Cell proliferation and viability assays

1 mL of cell suspensions were taken from spinner flasks and washed twice with PBS. The microcarrier was incubated overnight in a low permeability crystal violet solution containing 0.1 M citric acid. To determine cell counts, the liquid was thoroughly mixed using a pipette and then transferred to a haemocytometer to count the number of viable nuclei present. Subsequently, cells were stained with the Calcein-AM/PI Live/Dead Cell Double Staining Kit (40747ES80, Yeasen) following the manufacturer's instructions. Subsequently, cells were examined under a fluorescent inverted microscope to visualize green and red fluorescence.

Cell-microcarrier aggregation analysis

500 μL of cell suspensions were taken from spinning flasks, and imaged using a Nikon microscope. To accurately determine the size of aggregates formed by cells and microcarriers, the area and diameter of

each aggregate were quantified using ImageJ software. Results were compiled to create a statistical map illustrating the size distribution of the cell-microcarrier aggregates under specific culture conditions.

Flow cytometry assay

The surface phenotype of hUC-MSCs was characterized using flow cytometry. hUC-MSCs attached to the cell culture flask or microcarriers were digested using a 0.25% trypsin solution. The resulting cell suspension was collected through a cell strainer. Cells were resuspended in a staining buffer composed of 0.1% NaN_3 and 1% BSA in PBS. Cells were incubated with different cell surface antibodies for 30 minutes, including CD14, CD34, CD45, CD73, CD90, CD105, and isotype controls. Flow cytometry analysis was performed using a Beckman CytoFLEX instrument, and data was captured from a minimum of 10,000 cells per sample. FlowJo software was utilized for data analysis to determine the percentage of cells expressing each cell surface antigen.

RNA extraction and quantitative reverse transcription polymerase chain reaction (qRT-PCR)

Total RNA of hUCMSCs was extracted using TRNzol Universal. The extracted RNA was quantified using a microvolume spectrophotometer. To synthesize cDNA, 1 μg of RNA was added to a reverse transcription premix (11141ES60, Yeasen). qRT-PCR was performed using a BIO-RAD CFX96 fluorescence quantitative PCR instrument. Amplification was carried out for 40 cycles using SYBR Green premix (11184ES08, Yeasen). The relative expression levels of specific genes were calculated using the $2^{-\triangle\triangle CT}$ method, with triplicates performed for each sample. Gene-specific primers were designed using the Primer-BLAST tool provided by the NCBI.

CFD Simulation

This study aimed to simulate and investigate the fluid dynamic characteristics generated by the rotation of two different impellers in commercial spinner flasks. The container and impeller structures are shown in Fig. 1. The simulation settings, including rotational speed and working volume, closely matched the experimental conditions, and a total of 8 operating conditions were simulated.

The fluid flow inside spinner flasks was simulated using water at a temperature of 37℃. The water had a density of 0.998 g/cm^3, a dynamic viscosity of 7.01×10^{-4} Pa●s. To accurately simulate the flow patterns inside a bioreactor, the computational domain was divided into two parts: a rotating body known as the rotor, and a stationary body known as the stator. The rotor and stator were not physically separated, and their interaction was measured using the sliding mesh technique.

The mesh for simulations was generated using ANSYS Meshing, employing unstructured grids. Boundary layers were captured using the inflation layer method. The number of elements created varied, ranging from approximately 4×10^5 to 12×10^5 elements, with grid independence confirmed using the impeller torque. All operating conditions were simulated and analysed using approximately 8×10^5 elements.

The two impellers used in these simulations had maximum diameters of 44 mm and 48 mm, respectively. The impeller Reynolds numbers generated at different speeds ranged from 1000 to 3000, indicating that the fluid flow inside the spinner flasks falls within the range of moderate turbulence(Venkat et al. 1996). Turbulence modelling was performed using the k-ω SST model (Menter 1994), which takes into account the effects of turbulent shear stress. The standard k-ω model was used in the near-wall region, while the standard k-ε model was employed in the bulk liquid region to enhance the accuracy of the simulation results.

The commercial software ANSYS Fluent 2021R1 (ANSYS Inc., Canonsburg, PA, USA) was utilized to determine the governing equations. The coupling between pressure and velocity fields in the flow domain was predicted using the SIMPLE algorithm. The impeller and shaft were modelled as rotating walls, while all other surfaces were considered to have a no-slip boundary condition. Since no deformation of the free surface was observed during the experimental process, the top surface of the model was assigned as a planar wall with zero shear to serve as the gas-liquid contact interface.

Convergence of the simulation was determined based on iteration residuals less than 10^{-4} and a stable impeller torque. The time step was selected to ensure a rotation of the impeller by 0.9° during each step. To obtain velocity and shear rate distributions, all cases were simulated with ten complete revolutions. The temporal-averaged values for velocity and shear rate were calculated based on data from the last four rotations.

Numerical flow characteristics

The Q_z can be characterized by integrating the axial velocity over the cross-section at a specific height within the spinner flask. As a result of mass conservation in the flow field, the positive and negative axial pumping rates are equal, giving rise to the following equation:

$$Q_z = \int_{\Lambda} V_Z^+ \mathrm{d}A = \int_{\Lambda} V_Z^- \mathrm{d}A$$

In which, V_Z^+ and V_Z^- represent the positive and negative axial velocities, respectively, and A is the cross-sectional area at a specific height within the spinner flask.

By integrating the Q_z with respect to the liquid level height (H), the average axial pumping rate (Q_{zave}) can be obtained as follows:

$$Q_{\mathrm{zave}} = \frac{1}{H}\int_0^{\mathrm{H}}\int_{\mathrm{A}} V_{\mathrm{Z}}^+ \mathrm{d}A\mathrm{d}H = \frac{1}{H}\int_0^{\mathrm{H}}\int_{\mathrm{A}} V_{\mathrm{Z}}^- \mathrm{d}A\mathrm{d}H$$

SSR can be calculated using the velocity components V_x, V_y and V_z with the following equation:

$$SSR = 2\left\{\begin{array}{c}\left[\left(\frac{\partial V_x}{\partial x}\right)^2+\left(\frac{\partial V_y}{\partial y}\right)^2+\left(\frac{\partial V_z}{\partial z}\right)^2\right]+\\ \left[\left(\frac{\partial V_x}{\partial y}+\frac{\partial V_y}{\partial x}\right)^2+\left(\frac{\partial V_x}{\partial z}+\frac{\partial V_x}{\partial x}\right)^2+\left(\frac{\partial V_y}{\partial z}+\frac{\partial V_y}{\partial z}\right)^2\right]\end{array}\right\}^{1/2}$$

Statistical analyses

Statistical analysis was performed using GraphPad Prism version 8. Data analysis was conducted using t-tests and one-way ANOVAs. A p-value less than 0.05 indicated a statistically significant difference between groups.

Results and Discussions

Effect of Rotational speed on the cell-microcarrier aggregate size

Microcarriers inoculated with cells tend to form aggregates during the culture process. In this study, we investigated the effect and pattern of rotational speed on the formation of cell-microcarrier aggregates using four different speeds (30, 45, 60, and 75 rpm) (Fig. 2). On day 1, all microcarriers were dispersed individually in a liquid medium. As cells proliferated and migrated on the microcarrier surface, aggregation was observed. Microcarriers started to adhere and form aggregates at 30 rpm and 45 rpm on day 5, while no significant clustering of microcarriers occurred at 60 rpm and 75 rpm. By the 9^{th} day of culture, a large number of cells wrapped around the surface of the microcarriers, forming tight aggregates (Fig. 2A). Quantitative analysis of aggregate size in the culture flasks (Fig. 2B) revealed a significant increase in aggregate size from day 5 onwards at 30 rpm and 45 rpm. However, this phenomenon was not observed until day 7 at 60 rpm and 75 rpm. Higher rotational speeds may have reduced cell migration between microcarriers or decreased their contact frequency due to the increased suspension of microcarriers, thereby slowing down aggregate formation. The average diameter of aggregates formed at the lowest rotational speed was significantly higher at 3.36 ± 0.94 mm compared to the other groups. Similarly, larger aggregates of 1.99 ± 0.69 mm were formed at 45 rpm. Speeds below 45 rpm were considered low speeds, while speeds above 45 rpm were considered high speeds. Significantly smaller aggregates were formed at high speeds compared to low speeds, with diameters of 0.52 ± 0.09 mm and 0.51 ± 0.10 mm, respectively (Fig. 2C). Histograms of diameter distributions further reflected the size and distribution homogeneity of aggregates (Fig. 2D). Aggregates ranging from 1-6 mm was observed at 30 rpm, while aggregates ranging from 1-4 mm were seen at 45 rpm, indicating a wider distribution range. In contrast, aggregates formed at higher rpm had smaller diameters and a more homogeneous distribution. In summary, the size of cell-microcarrier aggregates during suspension culture was influenced by the stirring speed. Larger aggregates were formed at low speeds, while high speeds resulted in smaller and more homogeneous size distributions. There appeared to be a rotational speed threshold between 45-60

rpm, at which aggregate size began to stabilize. However, the exact effect of this threshold on hUC-MSCs culture warrants further investigation.

Cell proliferation and function in spinner flasks

Subsequently, this study evaluated the impact of rotational speeds on cell viability and proliferation. A significant number of viable green fluorescent cells were observed on the surface of aggregates in each group, with minimal red fluorescent dead cells . This indicated that cells on the surface of aggregates exhibited good viability regardless of the rotational speed (Fig. 3A). Upon slicing the 3 mm aggregates formed under 30 rpm, a few dead cells were observed, suggesting a possible decrease in cell vitality within the center of aggregates due to limited substance transfer. Since the aggregates formed under other rotational speeds were smaller than 1 mm, it was difficult to slice them, and there is little possibility of mass transfer limitation. Consequently, cells at the center of aggregates were not visualised. Strategies for cell expansion generally aim to prevent the formation of aggregates larger than 1 mm since they are prone to diffusion restrictions, sedimentation, and hindered survival of inner cells. Moreover, larger aggregates also impede subsequent cell digestion, separation, and homogeneous suspension in the reactors. As observed in a study by Luo *et al.*(Luo et al. 2014), the viability of cells significantly decreased beyond 500 μm from the tissue surface when constructing large-sized engineered tissues using Cultispher S. Thus, the formation of aggregates with a diameter smaller than 1 mm is crucial to prevent inner cell death caused by hindering mass transfer.

Fig. 3B demonstrates the variation in cell densities and aggregate sizes with culture time at different rotational speeds. Under 30 rpm and 45 rpm, the cell density reached its peak on the 5th day, with a respective count of $41.25\pm5.10\times10^4$ and $40.45\pm3.54\times10^4$ cells/mL before gradually declining. On the other hand, at 60 rpm and 75 rpm, the highest cell density was achieved on the 7th day, measuring $36.20\pm1.96\times10^4$ and $31.95\pm3.68\times10^4$ cells/mL, respectively, which were lower than the peak densities observed under lower rotational speeds. Analysing the pattern of changes in aggregate size, it appeared that the decrease in cell density at higher rotational speeds could be attributed to two primary factors: (1) The adhesive forces between cells and the extracellular matrix, akin to bonding materials, can cause microcarrier agglomeration, thereby providing more growth space within the aggregates(Caruso et al. 2014). Increased rotational speed reduces microcarrier aggregation, thus partially reducing cell density. (2) Higher stirring speeds intensify fluid flow, leading to increased shear stress on the cells. This excessive shear stress can adversely affect the viability and proliferation of MSCs, and even result in cell detachment from the microcarriers(Maul et al. 2011). Assessing the phenotypic characteristics of expanded cells (Fig. 3C), hUC-MSCs maintained their characteristic surface markers, with CD73 and CD90 positivity rates above 99%, which showed no significant difference compared to pre-expansion levels. Although the CD105 positivity rate remained above 95%, it decreased slightly in comparison to the pre-expansion value. This decline could be attributed to the prolonged enzymatic digestion during the cell harvesting process from the microcarriers and the fluid shear imposed during stirring. Importantly, this reduction in phenotype expression was found to be reversible(dos Santos et al. 2014).

The fluid shear generated by the stirring speed affected various biological functions of cells, including cell proliferation and differentiation potential. The expression of stemness genes in cells under different stirring speeds was examined using qRT-PCR. As shown in Fig. 4A, the relative expression levels of stemness markers *SOX2*, *OCT4*, and *Nanog* were highest at 30 rpm. As the stirring speed increased, the relative expression levels of stemness genes significantly decreased. Furthermore, quantitative analysis of differentiation-related genes revealed that the relative expression of *Runx2*, a key regulator of osteogenic differentiation, was lower at 30 rpm and 45 rpm, while it was significantly upregulated with increasing stirring speed. Similarly, the relative expression level of *PPAR-γ*, a key gene involved in adipogenic differentiation, showed an increasing trend with higher stirring speeds (Fig. 4B). In summary, as the stirring speed increased, the stemness of cells cultured on microcarriers decreased, and spontaneous differentiation occurred. Several studies have reported that fluid shear stress can induce cell differentiation. Compared to static cultures, the application of shear stress has been shown to promote osteogenic differentiation of MSCs in both 2D and 3D environments(Yue et al. 2019; Elashry et al. 2021). Similarly, appropriate shear stress stimulation is beneficial for the adipogenic differentiation of cells(Adeniran-Catlett et al. 2016). Therefore, shear stress is advantageous in certain differentiation strategies. However, for expansion strategies aimed at harvesting stem cells, shear stress should be minimized to prevent unnecessary differentiation.

The experimental results mentioned above revealed a contradiction between the formation of millimetre-scale aggregates at low stirring speeds and the reduction in stemness associated with high stirring speeds. Although the 30 rpm condition demonstrated better expansion efficiency and superior stemness, the larger aggregates posed difficulties in cell harvesting, often necessitating higher enzyme concentrations and longer digestion times(Caruso et al. 2014). Furthermore, the heterogeneity of cells both inside and outside of the aggregates, especially in terms of differential gene expression, is a concern that needs to be addressed during the expansion of seed cells(Sart et al. 2020). The strategy of reducing aggregate size by increasing the stirring speed fails to meet the requirements of both cell proliferation and stemness maintenance. At 45 rpm, the stemness of cells no longer satisfied the demands of seed cell expansion, and the average aggregate size remained at 1.99 mm, thereby affecting cell digestion. While studies have explored the use of fresh microcarriers to delay aggregate formation, the increased friction and collision resulting from the higher microcarrier concentration can also contribute to cell death(Cherry and Papoutsakis 1986; Sion et al. 2020). Therefore, the goal of this study was to control aggregate size (less than 1 mm) to minimize mass transfer limitations and facilitate cell harvesting, while increasing cell density and maintaining higher stemness when compared to the control group. Achieving this required a more in-depth analysis of the fluid dynamics inside the bioreactor using CFD simulations, which can provide valuable insights for developing targeted improvement strategies.

Simulation of the flow field inside spinner flasks

To gain a deeper understanding of the formation process of microcarrier aggregates, the flow field inside the bioreactor was comprehensively analysed through a combination of experimental observations and CFD simulations (Fig. 5). The distribution of microcarriers during cell expansion could be directly

observed visually (Fig. 5A). On the 1st day of cell seeding, no aggregation of microcarriers was observed, and insufficient cell suspension occurred in bioreactors operating at 30 rpm and 45 rpm. A large number of microcarriers settled at the bottom of the bioreactors, especially at the center. By the 9th day, only large aggregates were found to accumulate beneath the impeller, with no suspended microcarrier particles present in the supernatant. At 60 rpm and 75 rpm, the microcarriers at the initial stage of cultivation were well suspended in the culture medium, but partial particle accumulation was observed in the bioreactor operated at 60 rpm during the later stages of cultivation. These results indicated that sedimentation issues of varying degrees existed in the bioreactor at speeds below 60 rpm. Additionally, CFD simulation displayed velocity profiles along the vertical plane of the original impeller at the four different speeds, overlaid with velocity vectors to better observe the distribution and organization of vortices within the spinner flask space (Fig. 5B). Multiple clockwise or counterclockwise vortices were observed within the reactor, primarily located under the shaft and blades, to the right side of the blades, and near the free surface. The positions and sizes of these vortices varied at different speeds but did not decrease in number, consistent with previous reports in the literature(Ghasemian et al. 2020). As expected, maximum velocity was observed at the top of the blades, while the flow velocity was lower at the bottom of the stirrer shaft, with the presence of vortices. The microcarriers may have been trapped in this region, leading to the formation of larger aggregates. A hemispherical bulge was present at the center of the bottom to reduce microcarrier retention, but based on actual observations, microcarrier aggregation could not be reduced at lower stirring speeds.

The results of the SSR contour maps in Fig. 5C were similar to that of the velocity contour maps, with the highest shear rate also occurring at the end of the blades, where they may pose a risk to cells. To further quantify the distribution of shear rates inside the bioreactor, time-averaged shear rate distribution maps for the entire computational domain within four rotations of the impeller were plotted at different speeds (Fig. 5D). As the rotational speed increased, the distribution of SSR moves to higher values. There was no significant difference in the peak shear rate distribution across different speeds, indicating that increasing the speed did not improve the homogeneity of the flow field. This may be due to the similarity in flow field structures at different speeds. Using simulation studies, Berry *et al.*(Berry et al. 2016) found that particles experienced intermittent shear forces of 0.1 to 0.5 Pa during flow, which may be caused by microcarriers being trapped by vortices beneath blades and intermittently subjected to high shear forces at blade ends.

In a stirred bioreactor, the combined action of fluid circulation and shear forces forms the flow field structure. Macroscopically, in the radial flow field, the fluid is segmented into upper and lower regions by vortices, with stronger local circulation within each region and weaker interactions between regions. This increases the probability of particle collisions and promotes particle aggregation, which is unfavourable for particle suspension. On the other hand, in the axial flow field, the fluid is discharged downwards by the impeller blades, creating overall circulation from bottom to top within the reactor, reducing particle aggregation and favouring particle suspension(Loubiere et al. 2019). The strength of fluid circulation and the degree of particle suspension were strongly correlated and related to the axial fluid velocity, which can

be quantified using the Q_z, as shown below in Section 3.4 using a comparative analysis. Based on the analysis mentioned above, the flow field generated by the original impeller was similar to the radial flow, with the input energy dissipating into multiple vortices, which is unfavourable for microcarrier suspension cultures. Adjusting this speed did not change the overall flow field structure, which may also be the fundamental reason for the results obtained in Section 3.2. By referring to the characteristics of the Eppendorf Airlift, an axial-flow impeller, the advantages of the original impeller with a high swept volume ratio of the blade were retained, while the end of the blade was extended and modified with an arc to prevent excessive shear forces. Additionally, the blades were bent along the horizontal line at the end of the axis to create the modified impeller (MI), which redirected the fluid downwards during impeller rotation, thereby generating overall circulation. In order to ensure the same input power per unit volume, the diameter of the modified impeller (MI) needed to be slightly larger than that of the original impeller. The specific structural parameters are shown in Fig. 1C and the power number, flow number, and other structural characteristics of the two impellers are presented in supplementary Table S1.

Flow behavior with modified impeller

The flow field and shear force distribution generated by the MI at different rotational speeds were simulated using CFD, and the results were compared with the simulated results of the original impeller in Section 3.3. Unlike the original impeller, MI generates a flow pattern that is closer to axial flow: the fluid is discharged downwards by the curved blades of the impeller, colliding with the bottom of the container, and then circulating from bottom to top. Fig. 6A shows the flow field structure corresponding to axial flow, where a large vortex with a size close to the liquid level inside the flask dominated the flow, and a weaker small vortex near the bottom of the container was observed. There was no vortex at the bottom of the axis, but the fluid velocity was lower, which may result in the aggregation of microcarriers. Theoretically, in this flow field, microcarriers were more easily suspended and did not remain at the bottom region for an extended period, but this requires validation in subsequent experiments.

Fig. 6B illustrates the contour of SSRs generated by the MI, which is similar to the results in Section 3.3. The SSR was highest at the tip of the blades, and the SSR of the bulk liquid was two orders of magnitude lower than the maximum SSR. Table 1 summarizes the SSR_{ave} for both impellers at different rotational speeds. Since the input power per unit volume was substantially similar (supplementary Table S1), the SSR_{ave} of the original impeller was only approximately 15% higher than that of the MI at the same rotational speed. However, the distributions of SSR for the two impellers differed slightly (Fig. 6C). When the SSR was lower than the SSR_{ave}, the volumetric contribution of SSR was higher for the MI, indicated by a higher volume percentage (PV) value, suggesting that the homogeneity of the flow field created by the MI was slightly better than that of the original impeller.

The structural changes in the impeller had no significant impact on the distribution of the SSR but greatly enhanced the Q_z. Fig. 6D illustrates the distribution of the Q_z at different relative liquid levels. For both impellers, an increase in rotational speed led to an improvement in the Q_z at various heights. The highest Q_z values were concentrated around relative heights of 0.2 to 0.4, which corresponded to the lower-middle

section of the original impeller and the region below the bending line of the MI. The Q_z values at the liquid surface and bottom of the container were the smallest. However, at the same rotational speed, the Q_z generated by the MI is higher at different relative heights when compared to the original impeller, with the maximum value being approximately twice as high. Additionally, the Q_{zave} was 50% to 60% higher for the MI. The Q_{zave} generated by the MI at 45 rpm was comparable to that of the original impeller at 75 rpm. This indicated that the MI could suspend aggregates more uniformly at lower levels of SSR, which contributed to investigate the main factors influencing aggregate size.

Table 1. SSR_{ave} and Q_{zave} of two impellers at various rotational speeds. OI represents the original impeller, and MI represents the modified impeller.

Rotate speed (rpm)	30	45	60	75
SSR_{ave}-OI (s^{-1})	6.75	10.54	14.37	18.50
SSR_{ave}-MI (s^{-1})	6.06	9.19	12.72	16.16
Q_{zave}-OI (m^3/s)	2.40E-04	3.71E-04	5.33E-04	6.32E-04
Q_{zave}-MI (m^3/s)	4.00E-04	5.93E-04	7.99E-04	10.9E-04

Application of the MI to cell culture.

The MI was employed to cell culture. It was observed that the flow pattern created by the impeller was more suitable for the required microenvironment to expand hUC-MSCs, although further validation is necessary to confirm this finding. Under conditions similar to previous studies, the suspension capability of the new impeller was visually assessed in a spinner flask (Fig. 7A). Even at the lowest rotational speed of 30 rpm, the MI demonstrated the ability to effectively suspend microcarriers with no obvious deposition at the bottom of the flask on the 1^{st} day of culture. However, by the 5^{th} day, an increase in microcarrier clustering was evident at 30 rpm and 45 rpm, with aggregate deposition observed at 30 rpm. By the 9^{th} day, the majority of microcarriers were distributed in the lower half of the flask, although the suspension achieved with the MI was still superior to that achieved with the original impeller stirring. The MI at 45 rpm and higher rotational speeds ensured optimal suspension of the microcarriers. The quantification of the degree of aggregate suspension using the Q_z was found to be feasible.

Furthermore, the impact of the improved impeller stirring on the size of microcarrier aggregates was evaluated. After 9 days of MI culture, although dense aggregates surrounded by cells were still present, their size was significantly smaller compared to those formed under the original impeller conditions (Fig.s 2A and 7B). The diameter distribution of aggregates formed by the original and improved impellers demonstrated that the average aggregate diameter at 30 rpm decreased from 3.36±0.94 mm to

1.25±0.26 mm, representing only 37% of the original size. Similarly, the average diameter of aggregates at 45 rpm decreased from 1.99±0.68 mm to 0.87±0.18 mm. Under high-speed conditions of 60 rpm and 75 rpm, the diameter consistently remained below 0.5 mm. It is worth noting that as well as reducing the size of microcarrier aggregates, the distribution of aggregate sizes formed under the new impeller stirring was more uniform. These results indicated that optimizing the impeller structure to enhance aggregate suspension could effectively decrease the size of aggregates and promote a more homogeneous distribution.

These experimental results were further analysed by correlating the average aggregate size under different conditions with the simulated values of SSR_{ave} and Q_{zave}, in order to determine the crucial physical factors influencing aggregation. In previous studies, the size distribution of multicellular spheroids was often explained using the Kolmogorov vortex length, wherein the aggregate size is slightly smaller than the vortex length. The shear forces exerted by the vortices were considered the dominant factor influencing aggregate size(Ghasemian et al. 2020). The cell-microcarrier aggregates have a size range of 200 to 5000 μm, which is much larger than the distribution of Kolmogorov vortex length within the spinner flask (100-300 μm). Therefore, this method is not suitable for this study. Additionally, cell and microcarrier aggregates tend to accumulate at the bottom of the spinner flask at lower rotational speed, resulting in increased aggregate size. Hence, the degree of suspension should also be considered as one of the criteria for predicting aggregate size. Shear stress rate (SSR_{ave}) and suspension quality index (Q_{zave}) were quantified to represent the shear force and degree of aggregate suspension, respectively, and were plotted against the average aggregate size (Fig. 8A and Fig. 8B).

As illustrated in Fig. 8A,the average size of aggregates remained relatively constant once SSR_{ave} exceeded 14 s^{-1}. However, when SSR_{ave} was lower than 14 s^{-1}, significant differences in average aggregate size were observed between two impellers, indicating that SSR is not the sole determining factor for aggregate size.Fig. 8B depicts these data points were fitted with a power-law curve, indicating that Q_{zave} is the dominant factor in determining aggregate size .Notably, when the Q_{zave} fell below 6×10^{-4} m^3/s, the aggregates were not fully suspended (Fig. 5A and Fig. 7A), and their average size significantly decreased as the Q_{zave} increased. These findings indicated that in situations where aggregates were unevenly suspended, their average size was primarily determined by the degree of suspensionwhile shear forces play a minor role in this context. Overall, these results provide valuable guidance for expansion strategies of hUC-MSCs using microcarrier-based approaches. However, it is also important to consider other factors such as cell quantity and quality when evaluating the effectiveness of hUC-MSCs expansion.Comparing cell proliferation curves before and after modifying the impeller, it was observed that cell density increased under all rotational speeds, reaching its peak on the 7^{th} day (Fig. 7D). The most notable growth occurred at lower speeds, with the highest densities at 30 rpm and 45 rpm increasing from $41.25\pm5.10\times10^4$ and $40.45\pm3.54\times10^4$ cells/mL to $57.71\pm7.16\times10^4$ and $55.58\pm3.31\times10^4$ cells/mL, respectively. These results indicated that when the SSR_{ave} was less than 14 s^{-1}, the inhibitory effect of shear forces on cell growth was weaker. Furthermore, the improved suspension capability of

aggregates reduced their size, which may alleviate mass transfer limitations and enable an increase in cell quantity. However, under high-speed conditions, there was no significant improvement in the maximum cell density before and after impeller optimization. This could be attributed to the inhibitory effect of high SSR generated at high speeds on cell proliferation. The results of cell proliferation provide further evidence of the superiority of the MI in the expansion process of hUC-MSCs.

In order to investigate the potential impact of the MI on the differentiation potential of expanded cells, the expression of pluripotency genes and differentiation markers was evaluated (Fig. 9). The qRT-PCR results revealed that the use of the MI led to a significant upregulation of *SOX2*, *OCT4*, and *PPAR-γ* expression in MSCs at 30 rpm and 45 rpm. Under high-speed conditions, only *OCT4* expression was upregulated, while no significant differences were observed in *SOX2* and Nanog expression (Fig. 9A). Moreover, in comparison to the culture conditions with the original impeller, the utilization of the MI resulted in an overall reduction of the expression of the osteogenic differentiation regulatory gene *Runx2* and downregulation of the expression of the adipogenic differentiation gene *PPAR-γ* under high-speed conditions (Fig. 9B).The upregulation of pluripotency genes and downregulation of differentiation genes suggest that the MI was less likely to induce spontaneous cell differentiation, and the expanded cells maintained a robust level of stem cell pluripotency. The contrasting gene expression results indicated that both mass transfer limitations and shear forces influenced the maintenance of cell pluripotency. The enhanced shear forces inevitably led to the downregulation of pluripotency genes. However, an increase in the Q_z facilitated improved suspension of aggregates, resulting in smaller aggregate sizes and alleviating mass transfer limitations, thus partially counteracting the negative impact of shear forces on pluripotency gene expression. Overall, when considering factors such as highest cell density, aggregate size, and pluripotency maintenance, it was crucial to have a SSR_{ave} below 14 s^{-1} and a Q_{zave} above 6×10^{-4} m^3/s in order to achieve optimal conditions. Among these, only the MI with a rotational speed of 45 rpm fulfilled these criteria.

Conclusion

In this study, a combination of CFD simulations and cell culture experiments was used to address the limitations of original impellers on improving the cultivation efficiency of hUC-MSCs via rotational speed adjustments. To overcome this problem, the basic configuration of the impeller was modified by transforming the flow pattern from radial to axial, and by optimising its size, resulting in the development of an improved impeller design. Additionally, the operational speed was fine-tuned. Adapting the microenvironment created by the impeller to match the characteristics of the cells. Remarkably, when compared to the original impeller, the modified impeller successfully controlled the aggregate size to approximately 0.87 mm under identical culture conditions. Consequently, this led to a significant 40% increase in the maximum cell density, while simultaneously suppressing spontaneous cell differentiation. The key findings and implications of this study are summarized as follows:

- The excessive aggregation of hUC-MSCs on microcarriers in spinner flask reactors hinders the maintenance of optimal aggregate size and suspension efficiency while preserving cell functionality.

This issue arises from the presence of multiple vortices in the flow field, which limit the overall circulation of microcarriers, resulting in excessively large aggregate sizes. An improved impeller design was developed, aimed to enhance the suspension capability of aggregates and optimize the flow field structure. Remarkably, this modified impeller design exhibited excellent performance in cell cultivation. It effectively maintained cell pluripotency, achieved a lower aggregate size, and simultaneously enabled a higher cell density. Through experimentation, a rotational speed of 45 rpm was identified as the optimal operating speed for maximizing these desired outcomes.

- The strength of shear force exerted by the impeller was quantified using the SSR, while the capability of the impeller to suspend aggregates was measured by the Q_z, with higher values indicating a stronger ability to suspend aggregates and achieve a higher degree of suspension. When the aggregates were not fully suspended, there was a more pronounced relationship between the aggregate size and the degree of suspension, with a higher suspension degree correlating with smaller aggregate sizes. However, the association between shear force and aggregate size was relatively less significant.
- The viability and differentiation potential of hUC-MSCs are influenced by the combined effects of shear force and mass transfer limitations. Increased shear force results in decreased cell density and pluripotency. However, when exposed to comparable levels of shear force, smaller aggregate sizes promoted higher cell viability and pluripotency, particularly when mass transfer was not restricted. Further exploration is warranted to unravel the underlying mechanisms of these phenomena. These insights provide valuable guidance for optimizing cultivation strategies of hUC-MSCs on Cultispher-S microcarriers. Regardless of impeller design and rotational speed, attaining optimal cultivation outcomes in spinner flask reactors requires adequate environmental conditions that maintain a SSR_{ave} below 14 s^{-1} and a Q_{zave} above 6×10^{-4} m^3/s.

Abbreviations

hUC-MSCs,	Human umbilical cord-derived mesenchymal stem cells;
CFD,	computational fluid dynamics;
hMSCs,	human mesenchymal stem cells;
SSR,	shear strain rate (s^{-1});
Q_z,	axial pumping rate (m^3/s);
SSR_{ave},	mean shear strain rate across the entire spinner flask zone (s^{-1});
Q_{zave},	mean axial pumping rate across the entire spinner flask zone (m^3/s);
qRT-PCR,	quantitative reverse transcription polymerase chain reaction ;
V_Z^+,	positive axial velocity (m/s);
V_Z^-,	negative axial velocities(m/s);
A,	cross-sectional area at a specific height within the spinner flask (m^2);
H,	liquid level height (m);
V_x, V_y and V_z,	velocity components (m/s);
OI,	original impeller;
MI,	modified impeller;

Declarations

Acknowledgements

Not applicable.

Authors' contributions

BZ conceived the research idea, designed the experiments. BZ and QL performed the experiments, analyzed the data and drafted the manuscript. YZ and QY assisted in the experimental setup and data collection. GD provided valuable insights during the manuscript writing process. GD, YZ and WT revised the manuscript. All authors read and approved the final manuscript

Funding

This work was supported by grants from the National Key Research and Development Program of China (Grant No. 2018YFC1105800)

Availability of data and materials

Data will be made available upon reasonable request.

Declarations

Ethics approval and consent to participate

Not applicable.

Consent for publication

Not applicable

Competing interests

The authors declare that they have no competing interests.

Author details

State Key Laboratory of Bioreactor Engineering, East China University of Science and Technology, Shanghai 200237, China

References

1. Adeniran-Catlett AE, Weinstock LD, Bozal FK, Beguin E, Caraballo AT, Murthy SK (2016) Accelerated adipogenic differentiation of hMSCs in a microfluidic shear stimulation platform. Biotechnol Prog 32:440-446.
2. Alanazi A, Munir H, Alassiri M, Ward LSC, McGettrick HM, Nash GB (2019) Comparative adhesive and migratory properties of mesenchymal stem cells from different tissues. Biorheology.56:15-30.
3. Barberini DJ, Freitas NPP, Magnoni MS, Maia L, Listoni AJ, Heckler MC Landim-Alvarenga (2014) Equine mesenchymal stem cells from bone marrow, adipose tissue and umbilical cord: immunophenotypic characterization and differentiation potential. Stem Cell Res Ther 5:25.

4. Berry JD, Liovic P, Šutalo ID, Stewart RL, Glattauer V, Meagher L (2016) Characterisation of stresses on microcarriers in a stirred bioreactor. Appl Math Model.40:6787-6804.
5. Hassan MNFB, Yazid MD, Yunus MHM, Chowdhury SR, Lokanathan Y, Idrus RBH (2020) Large-scale expansion of human mesenchymal stem cells. Stem Cells Int 2020:9529465.
6. Caruso SR, Orellana MD, Mizukami A, Fernandes TR, Fontes AM, Suazo CAT (2014) Growth and functional harvesting of human mesenchymal stromal cells cultured on a microcarrier-based system. Biotechnol Prog 30:889-895.
7. Cherry RS, Papoutsakis ET (1986) Hydrodynamic effects on cells in agitated tissue culture reactors. Bioproc Biosyst Eng 1:29-41.
8. de Sá da Silva J, Severino P, Wodewotzky TI, Covas DT, Swiech K, Cavalheiro Marti L (2020) Mesenchymal stromal cells maintain the major quality attributes when expanded in different bioreactor systems. Biochem Eng J 161:9.
9. dos Santos F, Campbell A, Fernandes-Platzgummer A, Andrade PZ, Gimble JM, Wen Y (2014) A xenogeneic-free bioreactor system for the clinical-scale expansion of human mesenchymal stem/stromal cells. Biotechnol Bioeng 111:1116-1127.
10. Eibes G, dos Santos F, Andrade PZ, Boura JS, Abecasis MMA, da Silva CL, Cabral JMS (2010) Maximizing the ex vivo expansion of human mesenchymal stem cells using a microcarrier-based stirred culture system. J Biotechnol 146:194-197.
11. El Omar R, Beroud J, Stoltz J-F, Menu P, Velot E, Decot V (2014) Umbilical cord mesenchymal stem cells: the new gold standard for mesenchymal stem cell-based therapies? Tissue Eng Part B-Re 20:523-544.
12. Elashry MI, Baulig N, Wagner A-S, Klymiuk MC, Kruppke B, Hanke T, Wenisch S, Arnhold S (2021) Combined macromolecule biomaterials together with fluid shear stress promote the osteogenic differentiation capacity of equine adipose-derived mesenchymal stem cells. Stem Cell Res Ther 12:116.
13. Ferrari C, Balandras F, Guedon E, Olmos E, Chevalot I, Marc A (2012) Limiting cell aggregation during mesenchymal stem cell expansion on microcarriers. Biotechnol Progr 28:780-787.
14. Friedenstein A, Jakovlevich KVP, Kurolesova AI, Frolova GP (1968) Heterotopic transplants of bone marrow. Transplantation 6:230-247.
15. Ghasemian M, Layton C, Nampe D, zur Nieden NI, Tsutsui H, Princevac M (2020) Hydrodynamic characterization within a spinner flask and a rotary wall vessel for stem cell culture. Biochem Eng J 157:11.
16. Grégoire C, Lechanteur C, Briquet A, Baudoux É, Baron F, Louis E, Beguin Y (2017) Review article: mesenchymal stromal cell therapy for inflammatory bowel diseases. Aliment Pharm Therap 45:205-221.
17. Hoang DM, Pham PT, Bach TQ, Ngo ATL, Nguyen QT, Phan TTK, Nguyen GH, Le PTT (2022) Stem cell-based therapy for human diseases. Signal Transduct Tar 7:272.

18. Huang H, Young W, Chen L, Feng S, Zoubi ZMA, Sharma HS, Saberi H, Moviglia GA (2018) Clinical cell therapy guidelines for neurorestoration (IANR/CANR 2017). Cell Transplant 27:310-324.
19. Huang J, Zhang B, Dai G, Chen C, Yu H, Tian H (2022) Synergistic effects in coaxial mixers: the controlling strategy of the flow and shear. Chem Eng Technol 45:210-219.
20. Jiao F, Xu J, Zhao Y, Ye C, Sun Q, Liu C, Huo B (2022) Synergistic effects of fluid shear stress and adhesion morphology on the apoptosis and osteogenesis of mesenchymal stem cells. J Biomed Mater Res A 110:1636-1644.
21. Jo CH, Lee YG, Shin WH, Kim H, Chai JW, Jeong EC, Kim JE, Shim H (2014) Intra-articular injection of mesenchymal stem cells for the treatment of osteoarthritis of the knee: a proof-of-concept clinical trial. Stem Cells 32:1254-1266.
22. Jossen V, Schirmer C, Mostafa Sindi D, Eibl R, Kraume M, Pörtner R, Eibl D (2016) Theoretical and practical issues that are relevant when scaling up hMSC microcarrier production processes. Stem Cells Int 2016:4760414.
23. Kaiser S, Jossen V, Schirmaier C, Eibl D, Brill S, van den Bos C, Eibl R (2013) Fluid flow and cell proliferation of mesenchymal adipose-derived stem cells in small-scale, stirred, single-use bioreactors. Chem Ing Tech 85:95-102.
24. Lawson T, Kehoe DE, Schnitzler AC, Rapiejko PJ, Der KA, Philbrick K, Punreddy S, Rigby S (2017) Process development for expansion of human mesenchymal stromal cells in a 50L single-use stirred tank bioreactor. Biochem Eng J 120:49-62.
25. Lin H, Sohn J, Shen H, Langhans MT, Tuan RS (2019) Bone marrow mesenchymal stem cells: Aging and tissue engineering applications to enhance bone healing. Biomaterials 203:96-110.
26. Liu L, Yu B, Chen J, Tang Z, Zong C, Shen D, Zheng Q, Tong X, Gao C, Wang J (2012) Different effects of intermittent and continuous fluid shear stresses on osteogenic differentiation of human mesenchymal stem cells. Biomech Model Mechan 11:391-401.
27. Loubière C, Delafosse A, Guedon E, Chevalot I, Toye D, Olmos E (2019) Dimensional analysis and CFD simulations of microcarrier 'just-suspended' state in mesenchymal stromal cells bioreactors. Chem Eng Sci 203:464-474.
28. Luo H, Chen M, Wang X, Mei Y, Ye Z, Zhou Y, Tan W-S (2014) Fabrication of viable centimeter-sized 3D tissue constructs with microchannel conduits for improved tissue properties through assembly of cell-laden microbeads. J Tissue Eng Regen M 8:493-504.
29. Maul TM, Chew DW, Nieponice A, Vorp DA (2011) Mechanical stimuli differentially control stem cell behavior: morphology, proliferation, and differentiation. Biomech Model Mechan 10:939-953.
30. Menter FR (1994) Two-equation eddy-viscosity turbulence models for engineering applications. AIAA J 32:1598-1605.
31. Nienow AW, Hewitt CJ, Heathman TRJ, Glyn VAM, Fonte GN, Hanga MP, Coopman K, Rafiq QA (2016) Agitation conditions for the culture and detachment of hMSCs from microcarriers in multiple bioreactor platforms. Biochem Eng J 108:24-29.

32. Nienow AW, Rafiq QA, Coopman K, Hewitt CJ (2014) A potentially scalable method for the harvesting of hMSCs from microcarriers. Biochem Eng J 85:79-88.
33. Papaccio F, Paino F, Regad T, Papaccio G, Desiderio V, Tirino V (2017) Concise review: cancer cells, cancer stem cells, and mesenchymal stem cells: influence in cancer development. Stem Cell Transl Med 6:2115-2125.
34. Sart S, Tomasi RFX, Barizien A, Amselem G, Cumano A, Baroud CN Mapping the structure and biological functions within mesenchymal bodies using microfluidics. Sci Adv 6:eaaw7853.
35. Schirmaier C, Jossen V, Kaiser SC, Jüngerkes F, Brill S, Safavi-Nab A, Siehoff A, van den Bos C, Eibl D, Eibl R (2014) Scale-up of adipose tissue-derived mesenchymal stem cell production in stirred single-use bioreactors under low-serum conditions. Eng Life Sci 14:292-303.
36. Sharma RR, Pollock K, Hubel A, McKenna D (2014) Mesenchymal stem or stromal cells: a review of clinical applications and manufacturing practices. Transfusion 54:1418-1437.
37. Simaria AS, Hassan S, Varadaraju H, Rowley J, Warren K, Vanek P, Farid SS (2014) Allogeneic cell therapy bioprocess economics and optimization: Single-use cell expansion technologies. Biotechnol Bioeng 111:69-83.
38. Simões IN, Boura JS, dos Santos F, Andrade PZ, Cardoso CMP, Gimble JM, da Silva CL, Cabral JMS (2013) Human mesenchymal stem cells from the umbilical cord matrix: Successful isolation and ex vivo expansion using serum-/xeno-free culture media. Biotechnol J 8:448-458.
39. Sion C, Loubière C, Wlodarczyk-Biegun MK, Davoudi N, Müller-Renno C, Guedon E, Chevalot I, Olmos E (2020) Effects of microcarriers addition and mixing on WJ-MSC culture in bioreactors. Biochem Eng J 157:107521.
40. Venkat RV, Stock LR, Chalmers JJ (1996) Study of hydrodynamics in microcarrier culture spinner vessels: A particle tracking velocimetry approach. Biotechnol Bioeng 49:456-466.
41. Yue D, Zhang M, Lu J, Zhou J, Bai Y, Pan J (2019) The rate of fluid shear stress is a potent regulator for the differentiation of mesenchymal stem cells. J Cell Physiol 234:16312-16319.
42. Zeddou M, Briquet A, Relic B, Josse C, Malaise MG, Gothot A, Lechanteur C, Beguin Y (2010) The umbilical cord matrix is a better source of mesenchymal stem cells (MSC) than the umbilical cord blood. Cell Biol Int 34:693-701.
43. Zhang J, Peng Y, Guo M, Li C (2022) Large-scale expansion of human umbilical cord-derived mesenchymal stem cells in a stirred suspension bioreactor enabled by computational fluid dynamics modeling. Bioengineering-Basel 9:274.
44. Zwietering TN (1958) Suspending of solid particles in liquid by agitators. Chem Eng Sci 8:244-253.

Figures

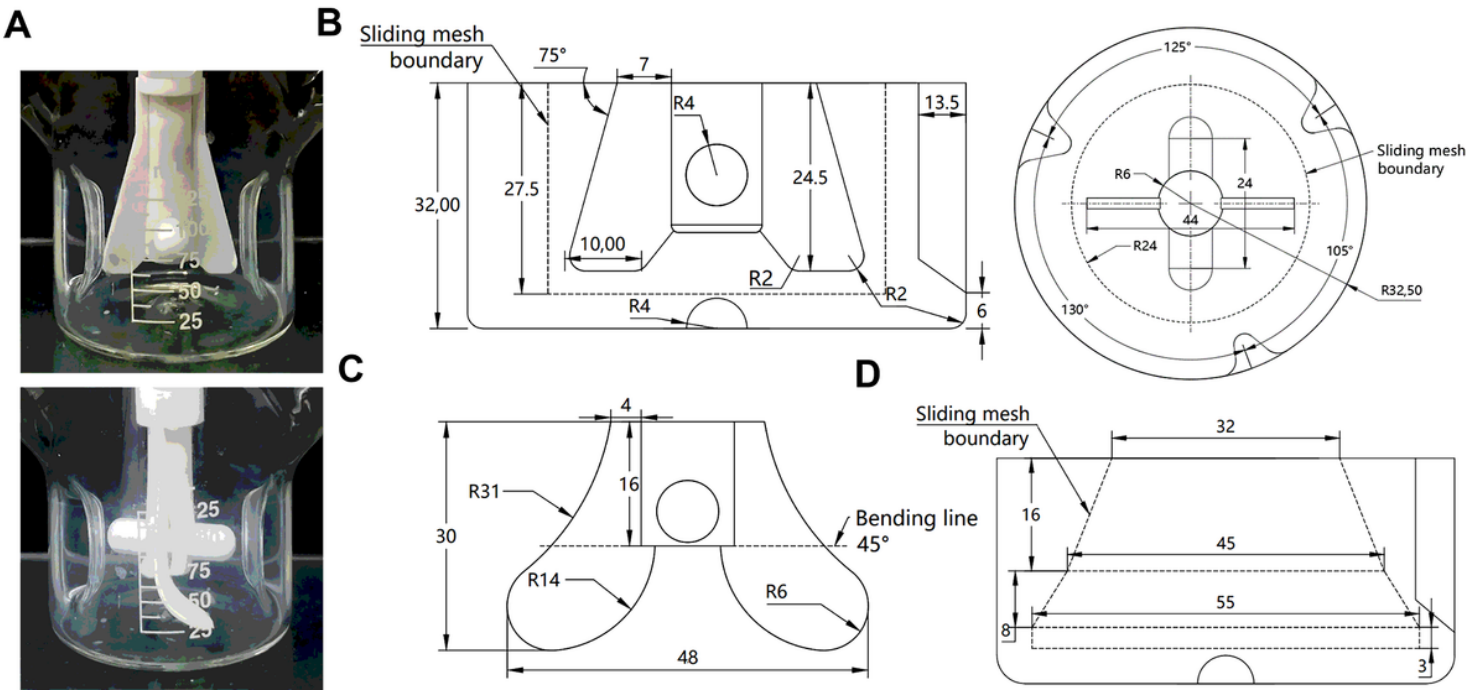

Figure 1

(A) A commercial spinner flask equipped with different impellers. (B) Vertical and horizontal cross-sections of the computational domain with the original impellers. (C) Structure and dimensions of the novel impeller before bending. (D) Structural parameters of the computational domain equipped with the novel impeller. All length measurements are in millimetres.

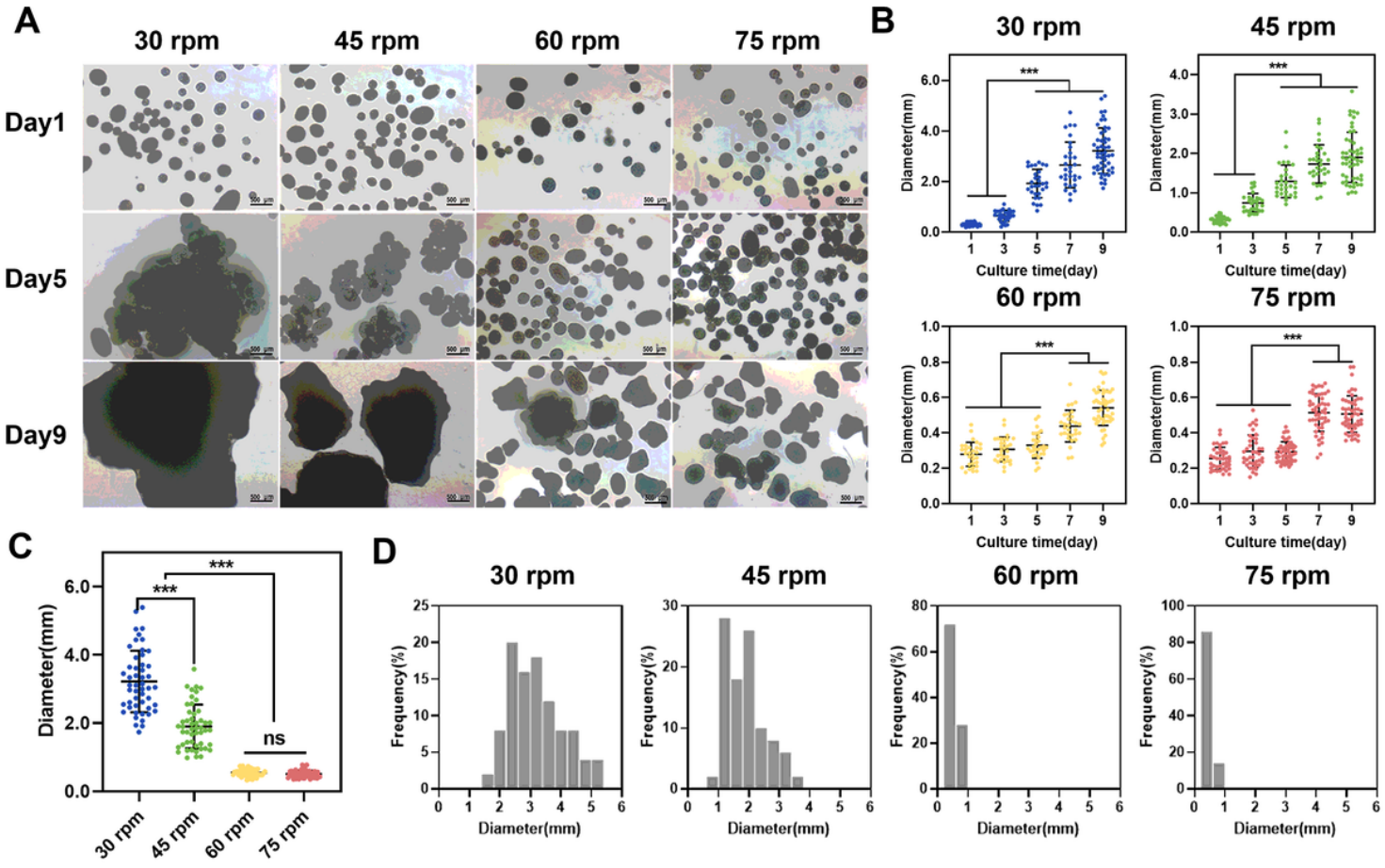

Figure 2

Cell-microcarrier aggregates at different rotational speeds. (A) Microscopic observation of cell-microcarrier cultures at different rotation rates after 1, 5 and 9 days of culture. Scale bar: 500 μm.(B) Changes in cell-microcarrier aggregate size with incubation times. (C) Comparison of aggregate sizes in rotovials at different rotational speeds at day 9. (D) Diameter distributions of cell-microcarrier aggregates.

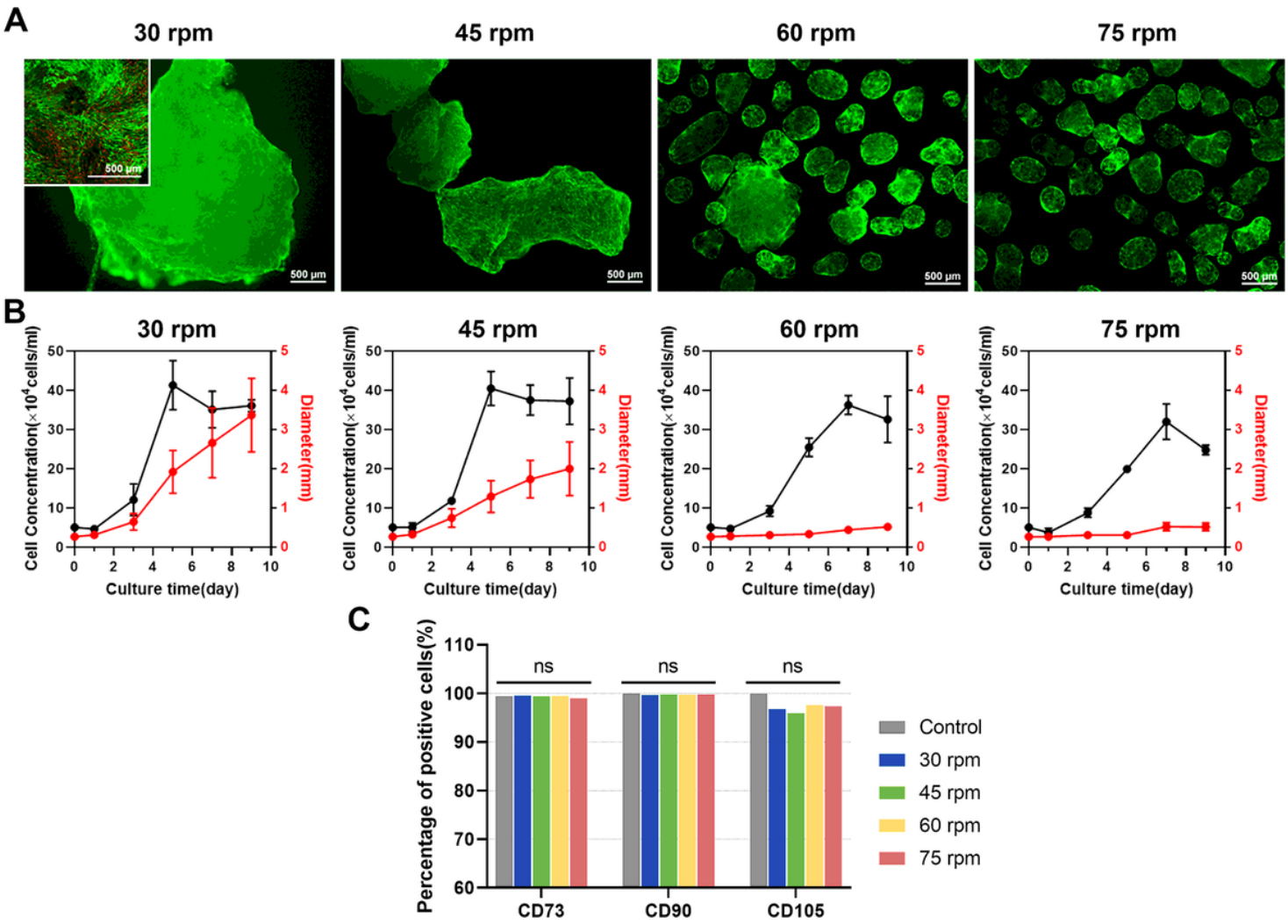

Figure 3

(A) Cell viability staining with Calcein-AM/PI on day 9 under different rotational speeds. Scale bar: 500 μm.(B) Dynamic curves of cell density and aggregate size. (C) Flow cytometry analysis of cell surface markers CD73, CD90, and CD105 at different rotational speeds. The control group consisted of pre-expansion cells.

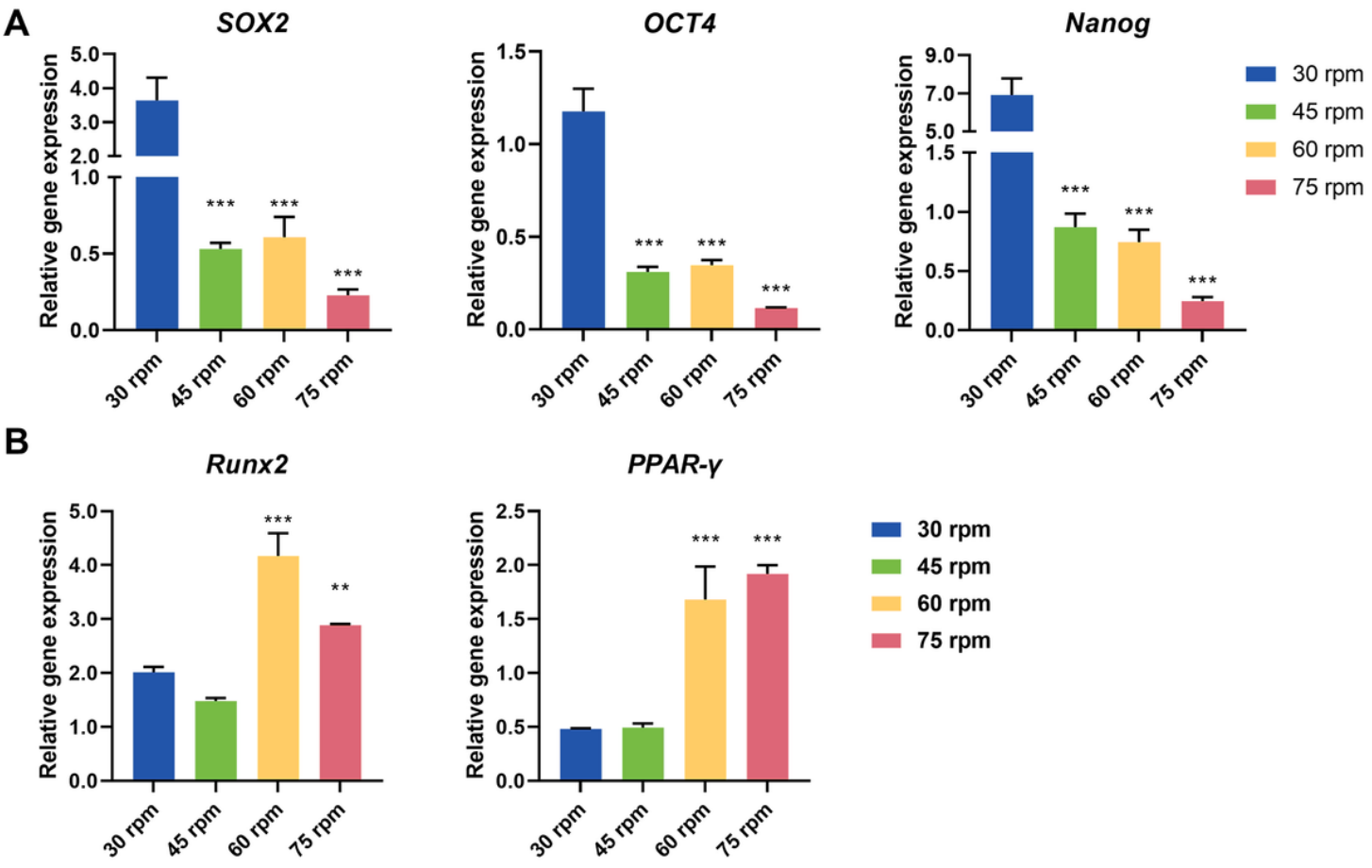

Figure 4

Relative expression levels of pluripotency genes (A) and differentiation marker genes (B).

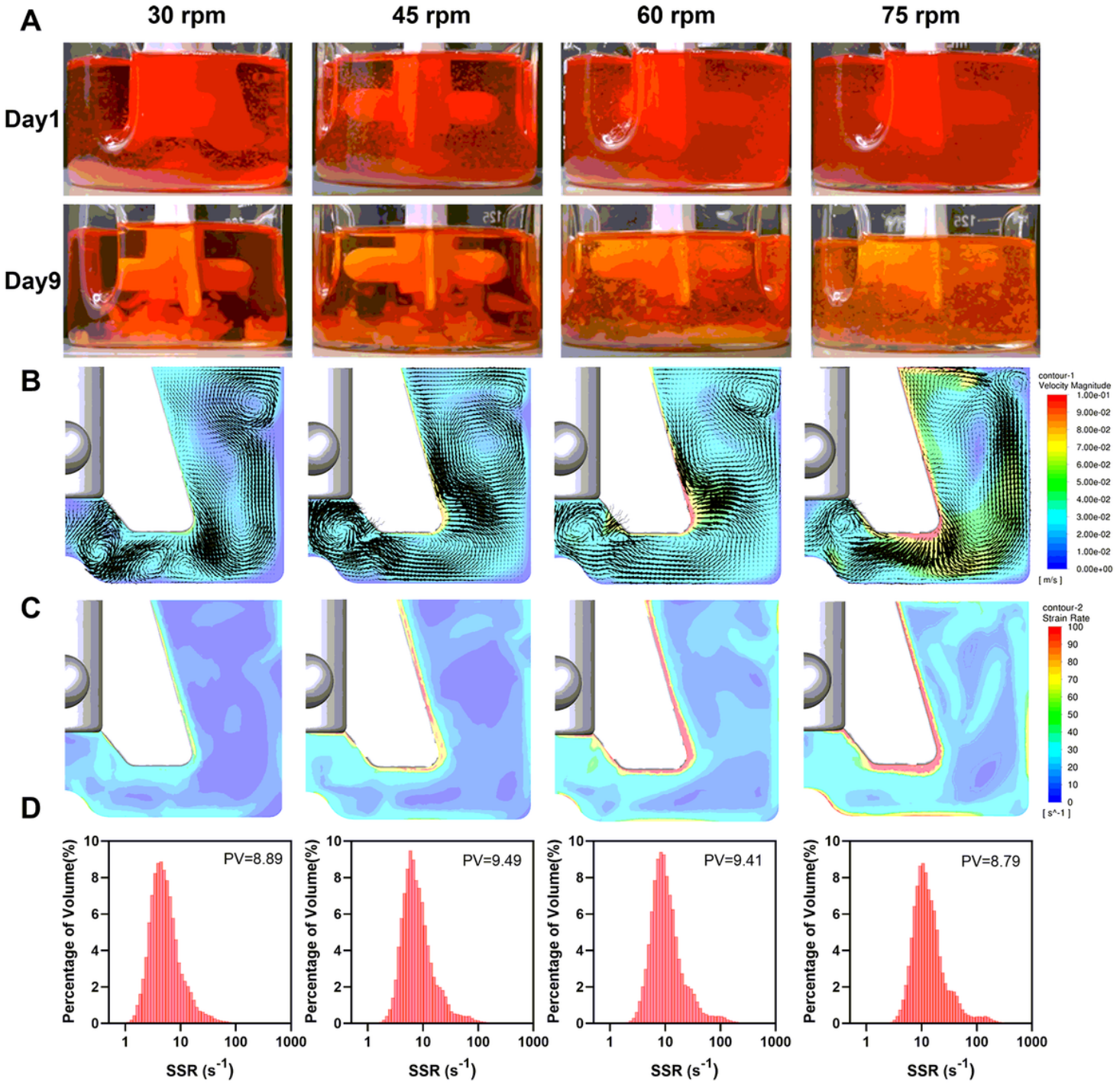

Figure 5

Analysis and simulation of the flow field in spinner flasks equipped with the original impeller. (A) Suspension of aggregates under different rotational speeds on day 9 of incubation. (B) Contour of instantaneous velocity magnitude and vector plots. (C) Contour of SSRs. (D) Distribution of SSR values. PV represents peak value.

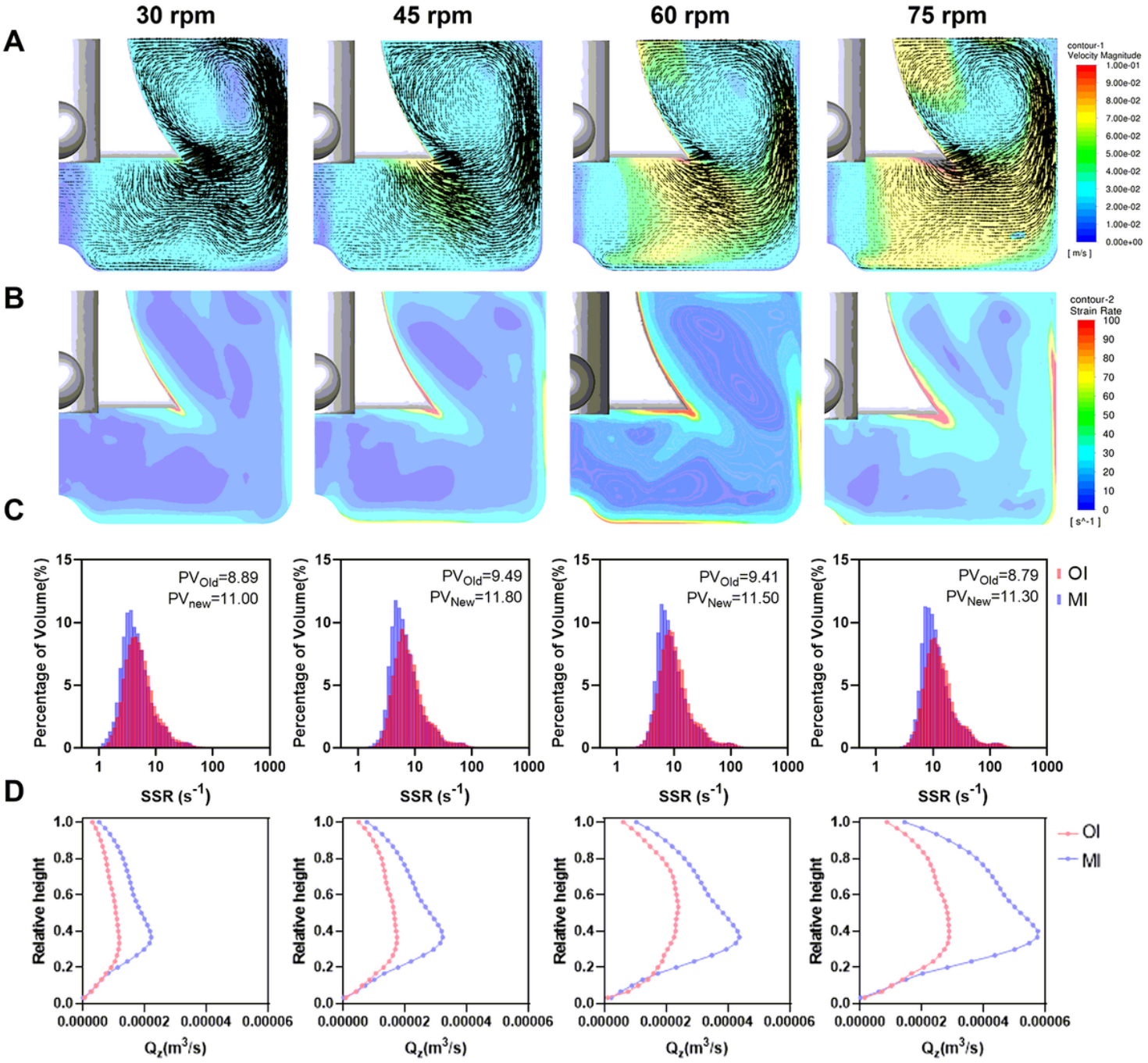

Figure 6

Analysis and simulation of the flow field in the spinner flask equipped with the MI. (A) Contour of instantaneous velocity magnitudes and vector plots. (B) Contour of SSRs. (C) Comparison of SSR distribution between the new and old impellers. PV represents peak value. (D) Comparison of Q_z distribution between the new and old impellers.

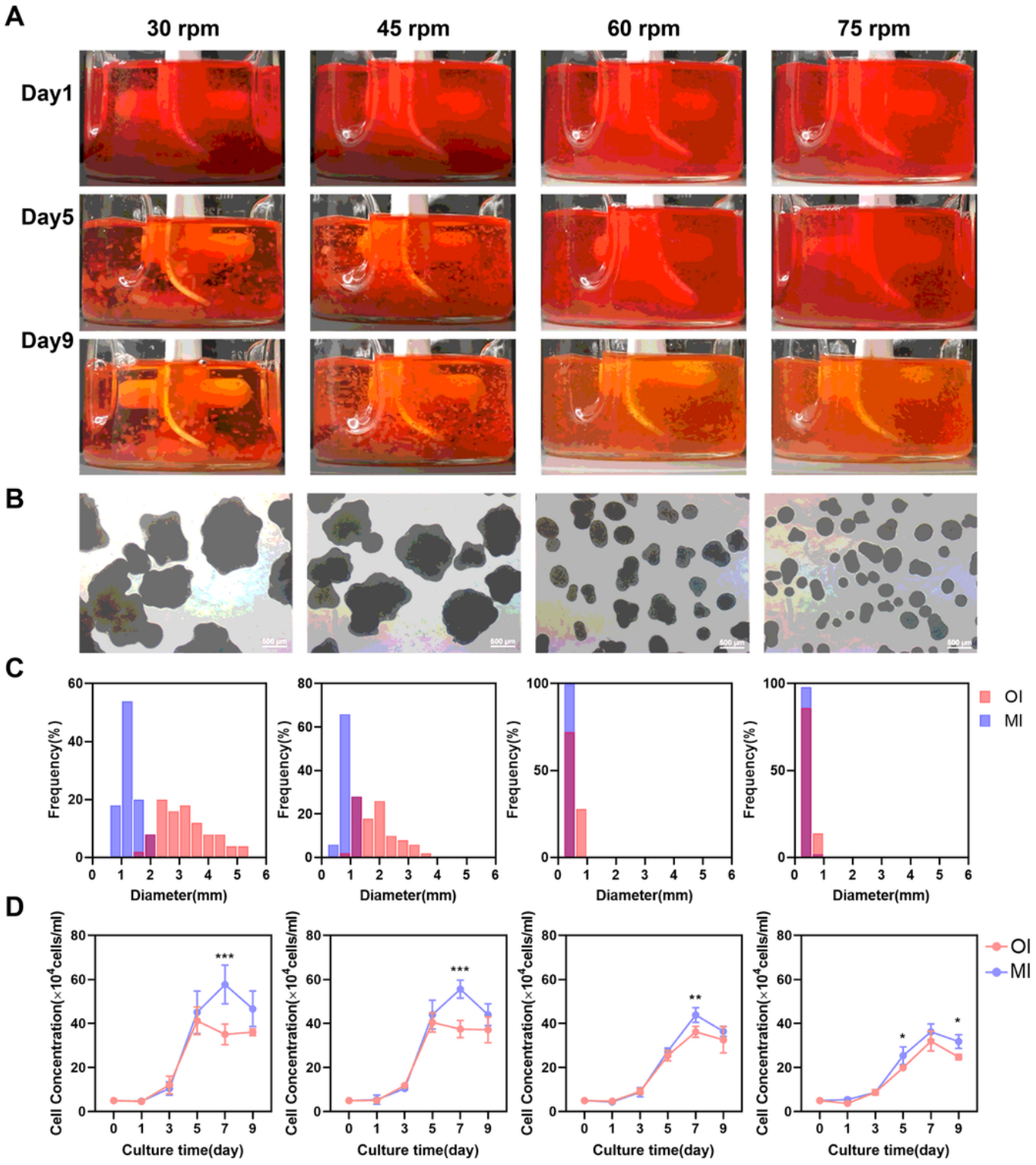

Figure 7

Influence of the MI on cell-microcarrier aggregate size and cell proliferation. (A) Suspension and distribution of microcarriers in flasks at days 1, 5, and 9 of culture. (B) Microscopic brightfield images of cell-microcarrier samples on day 9. Scale bar = 500 μm. (C) Comparison of the frequency distribution of cell-microcarrier aggregate diameters before and after impeller modification. Red: Original impeller (OI), Blue: Modified impeller (MI). (D) Cell proliferation curve before and after paddle leaf modification.

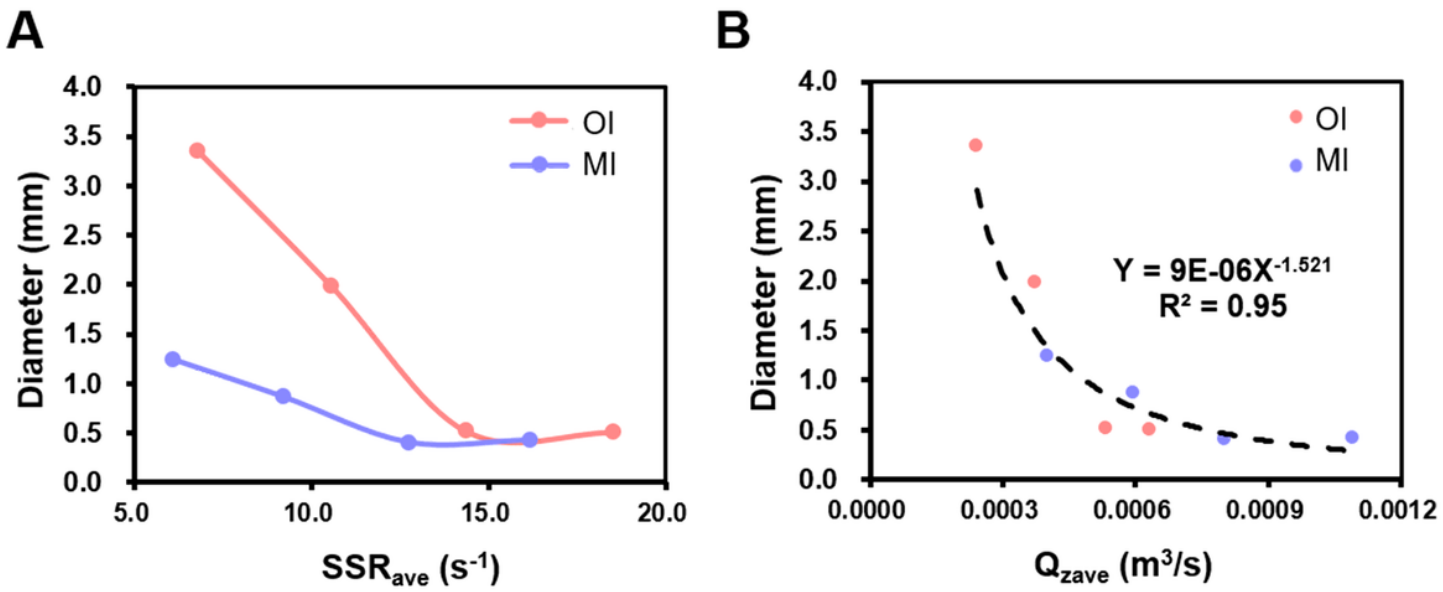

Figure 8

The effect of SSR_{ave} (A) and Q_{zave} (B) on the average size of aggregates.

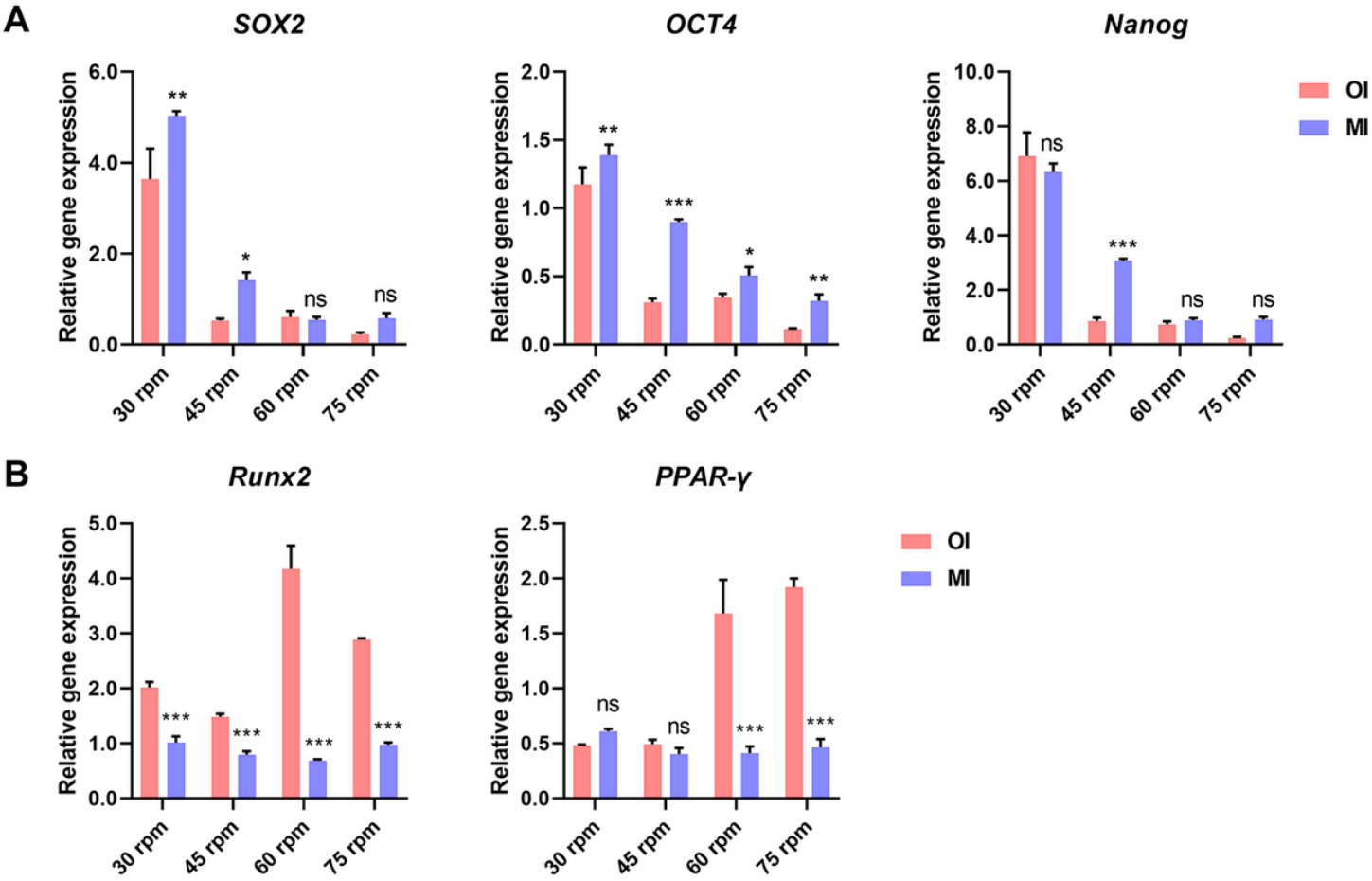

Figure 9

Influence of the MI on the expression of pluripotency (A) and differentiation genes (B) in cells.

Supplementary Files

This is a list of supplementary files associated with this preprint. Click to download.

- graphabstract.jpg
- supplementarymaterial.docx